

# An integrated model for the post-solidification shape and grain morphology of fusion welds

Anton Kidess<sup>a,d,\*</sup>, Mingming Tong<sup>b</sup>, Gregory Duggan<sup>b</sup>, David J. Browne<sup>b</sup>, Saša Kenjereš<sup>a,d</sup>, Ian Richardson<sup>c</sup>, Chris R. Kleijn<sup>a,d</sup>

<sup>a</sup>Department of Chemical Engineering, Delft University of Technology, Julianalaan 136, 2628BL Delft, Netherlands

<sup>b</sup>School of Mechanical and Materials Engineering, University College Dublin, Belfield, Dublin 4, Ireland

<sup>c</sup>Department of Materials Science and Engineering, Mekelweg 2, 2628CD Delft, Netherlands

<sup>d</sup>JM Burgers Centre for Fluid Mechanics, Mekelweg 2, 2628CD Delft, Netherlands

---

## Abstract

Through an integrated macroscale/mesoscale computational model, we investigate the developing shape and grain morphology during the melting and solidification of a weld. In addition to macroscale surface tension driven fluid flow and heat transfer, we predict the solidification progression using a mesoscale model accounting for realistic solidification kinetics, rather than quasi-equilibrium thermodynamics. The tight coupling between the macroscale and the mesoscale distinguishes our results from previously published studies.

The inclusion of Marangoni driven fluid flow and heat transfer, both during heating and cooling, was found to be crucial for accurately predicting both weld pool shape and grain morphology. However, if only the shape of the weld pool is of interest, a thermodynamic quasi-equilibrium solidification model, neglecting solidification kinetics, was found to suffice when including fluid flow and heat transfer.

We demonstrate that the addition of a sufficient concentration of approximately 1  $\mu\text{m}$  diameter TiN grain refining particles effectively triggers a favorable transition from columnar dendritic to equiaxed grains, as it allows for the latter to heterogeneously nucleate in the undercooled melt ahead of the columnar dendritic front. This transition from columnar to equiaxed growth is achievable for widely differing weld conditions, and its precise nature is relatively insensitive to the concentration of particles and to inaccurately known model parameters.

*Keywords:* welding, solidification, simulation, microstructure, Marangoni flow

---

## 1. Introduction

Welding is a ubiquitous industrial process of great economic and technological importance [1]. Welding processes involve complex physical phenomena spanning multiple length and time scales [2]. In particular, fusion welding processes involve phase changes, heat transfer by conduction, convection and radiation, as well as surprisingly strong fluid flow driven by Marangoni effects (gradients in surface tension), all of which are tightly coupled to one another.

Key mechanical properties of alloy welds are related both to (i) their shape and to (ii) their grain structure, and thus it is highly desirable to exert as much control as possible on both during weld formation. Whereas the shape is mainly determined by macroscopic phenomena such as heat transfer and Marangoni driven fluid flow during the

melting phase, and can be largely influenced by modifying the fluid flow through the addition of surface active species [3, 4], the grain structure is mainly determined by mesoscopic (grain scale) crystallization phenomena during solidification of the melt, and can be controlled by the addition of non-melting grain refining particles [5, 6, 7, 8, 9].

Typically, the grain morphology of a post-solidification weld consists of columnar dendrites, characterized by elongated, tree-like columns of solid which have grown into the melt. Equiaxed solidification, where solidification nucleation occurs within the melt away from the columnar front, is not common, as the thermal gradient ahead of the solidification front is too large to allow for the necessary undercooling for equiaxed growth to occur [6, 10]. However, the transition of the common columnar solidification mode to equiaxed solidification is of practical interest. Equiaxed material is less prone to the unwanted hot-cracking (tears appearing in the fusion zone near the end of the solidification process [11]) and also impedes the undesired segregation of alloying elements to the central plane of the weld [5, 7, 12].

Since quantitative experimental research of macroscopic shape evolution and mesoscopic structure evolution in

---

<sup>\*</sup>This manuscript has been published in the International Journal of Heat and Mass Transfer 85 (June 2015), doi:10.1016/j.ijheatmasstransfer.2015.01.144.

<sup>\*</sup>Corresponding author

Email address: A.Kidess@tudelft.nl (Anton Kidess)

## Nomenclature

$C$	Dendrite kinetics coefficient	$\vec{U}$	Fluid velocity
$C_0$	Alloy composition	$v$	Dendrite tip velocity
$c_p$	Heat capacity	$V_{equi}$	Volume of equiaxed dendrites
$\frac{D}{Dt}$	Material derivative	$V_{ex}$	Volume of existing equiaxed dendrites
$d_{min}$	Minimum diameter of nucleating particles	$V_{new}$	Volume of newly nucleated equiaxed dendrites
$D_l$	Diffusion coefficient of solute in the liquid	<b>Greek symbols</b>	
$F(d)$	Cumulative distribution function for equiaxed nucleation	$\alpha$	Partition coefficient
$\vec{F}_{damp}$	Momentum sink term due to solidification	$\epsilon$	Emmissivity
$f_s$	Volume fraction of solid in mush	$\eta$	Laser absorptivity
$g$	Volume fraction of solid	$\Gamma$	Gibbs Thomson coefficient
$h$	Convective heat transfer coefficient	$\gamma$	Surface tension
$k_q$	Gaussian distribution coefficient	$\gamma_{sl}$	Solid-liquid interfacial tension
$L$	Latent heat	$\lambda$	Thermal conductivity
$m$	Slope of the liquidus line	$\mu$	Dynamic viscosity
$N$	Count of nucleated particles	$\mu_{1/2}$	Median inoculant diameter
$P$	Laser power	$\phi_{col}$	Volume fraction of columnar dendrites
$p$	Pressure	$\phi_{equi}$	Volume fraction of equiaxed dendrites after taking into account grain impingement
$\dot{q}$	Heat flux	$\phi_s$	Volume fraction of mush
$R$	Volume averaged dendrite envelop radius	$\rho$	Density
$r_q$	$1/e^2$ radius for Gaussian distribution	$\rho_{seeds}$	Inoculant particle number density
$S_{latent}$	Latent heat source term	$\sigma_b$	Stefan Boltzman constant
$\Delta S_v$	Fusion entropy	$\sigma_d$	Standard deviation for the log-normal distribution of inoculant diameters
$T$	Temperature	<b>Subscripts</b>	
$\Delta T_c$	Local undercooling	$n$	Normal direction
$T_\infty$	Ambient temperature	$t$	Tangential direction
$T_s, T_l$	Solidus and liquidus temperature		

welds is tremendously difficult to conduct [13], there is a need for efficient, realistic numerical models that can predict both [14].

The majority of previously published numerical studies (e.g. [4, 15, 16, 17, 18]) on macroscopic phenomena during welding have focused on the evolution of the weld pool shape and temperature up to the end of the melt-

ing stage, and thus neglect further changes in the weld pool shape during re-solidification after the heat source has been removed. However, it has been shown that the shape of the weld pool can still change significantly during the subsequent re-solidification [19, 20]. A proper study of macroscopic weld formation should therefore include the solidification stage.

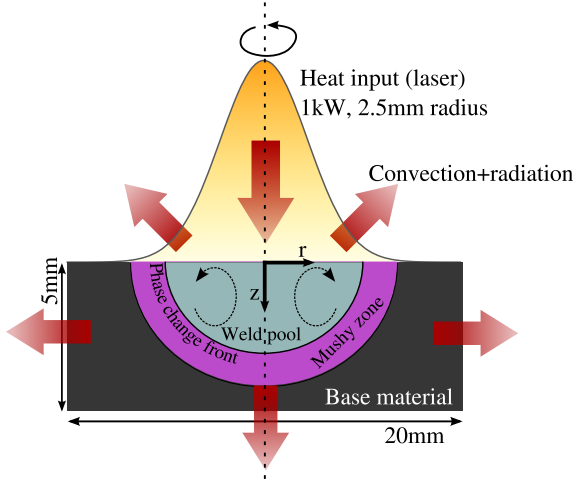


Figure 1: Schematic representation of the studied laser welding. The domain is assumed to be axisymmetric.

Other previous studies have focused on predicting the post-solidification mesoscopic grain structure of the weld, which is entirely determined during the solidification stage. In these studies the microstructure was either studied by a-posteriori analysis, neglecting undercooling of the melt and the possibility of heterogeneous nucleation sites (e.g. Zhang et al. [18]), or the solidification progression was modeled using mesoscopic models, while neglecting the influence of macroscopic phenomena such as fluid flow in the molten metal on the weld pool shape [5, 21, 22, 23, 24, 25].

However, the macroscale and the mesoscale cannot be separated, as macroscale phenomena such as fluid flow and heat transfer determine the evolution of solidification on the mesoscale as well. Therefore, a proper prediction of weld properties requires a combination of both types of modeling. In this paper we present such an integrated macroscale/mesoscale model and we show that it can be used to simultaneously predict the macroscopic shape and the mesoscopic grain structure of a solidified conduction-mode laser weld. On the macroscale, we compute the heat transfer and (thermocapillary driven) fluid flow in the weld. On the mesoscale, the solidification evolution is determined from actual interface kinetics, rather than interface equilibrium assumptions. With this integrated model, we investigate the role of fluid flow during solidification, and the possible alteration of the solidification mesostructure in a steel alloy laser weld using grain refining particles.

## 2. Mathematical formulation

### 2.1. Governing equations

A schematic of a typical stationary weld is shown in figure 1, where a non-moving slab of metal is targeted by a fixed high power laser. The laser irradiation will be absorbed by the target material, leading to an increase in temperature and eventually a melting phase change. Heat

will be transferred into the bulk of the welded material by conduction and convection. These phenomena are mathematically modeled with an energy transport equation with a source term for the latent heat of the phase change

$$\frac{D}{Dt}(\rho c_p T) = \nabla \cdot (\lambda \nabla T) + S_{latent} \quad (1)$$

Due to the non-uniform heating of the top surface, large temperature gradients will develop. These temperature gradients result in gradients in surface tension, leading to thermocapillary forces along the liquid-gas interface driving flow in the weld pool. The momentum transport is described by the Navier-Stokes equations, with a momentum sink that models the friction in the so-called mushy zone, where the liquid and solid phase co-exist

$$\frac{D}{Dt} \vec{U} = -\nabla p + \nabla \cdot (\mu \nabla \vec{U}) - \vec{F}_{damp} \quad (2)$$

In the following sections, we will first describe the mesoscale models used to determine the volume fraction of solid and the developing mesoscale structure during solidification, followed by a discussion of the source terms in equations 1 and 2, and their boundary conditions.

#### 2.1.1. Columnar dendrite growth

At the edge of the weld pool, columnar solidification starts instantaneously once the melt starts to be undercooled. To compute the growth of columnar dendrites, we follow the model by Browne and Hunt [26]. Here, the columnar dendrite front is depicted by a series of massless computational markers which can be thought of as an envelope that connects all dendrite tips (see figure 2). The markers are displaced explicitly perpendicular to the local columnar dendrite front, using an analytically determined local growth velocity:

$$v = C(\Delta T_c)^2 \quad (3)$$

$$C = \frac{-D_l}{8m(1-\alpha)C_0\Gamma} \quad (4)$$

The growth velocity  $v$  is dependent on the undercooling  $\Delta T_c = T_l - T$  and a kinetics coefficient  $C$ , which can be determined using analytical solutions of dendrite growth. Here, we use the model for  $C$  developed by Burden and Hunt [27] (equation 4), which is based on the hypothesis that structures grow near the optimum condition, with  $D_l$ ,  $m$ ,  $\alpha$ ,  $C_0$  and  $\Gamma$  the diffusion coefficient of solute in the liquid, the slope of the liquidus line, the partition coefficient, the alloy composition and the Gibbs Thomson coefficient, respectively. Alternative growth laws, such as the KGT model [28] based on the marginal stability criterion [29], may easily be incorporated.

The markers are initialized along the liquidus isotherm once the heat source is extinguished and solidification begins. If a given marker temperature exceeds the liquidus

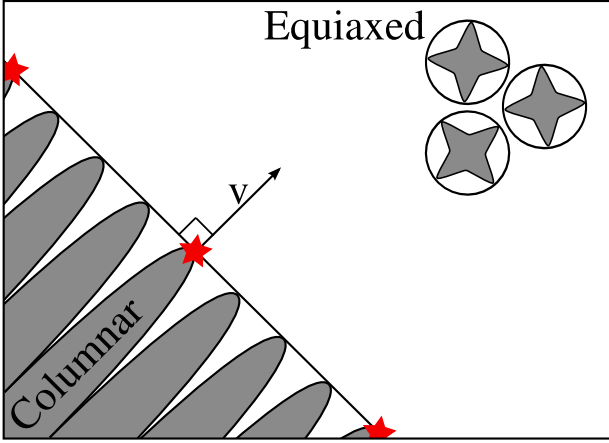


Figure 2: Schematic of the mushy zone at the mesoscale, with columnar dendrite tips, equiaxed dendritic grains and computational markers (stars with velocity  $v$ ) located at columnar dendrite tips

temperature due to remelting, it is reset to the closest liquidus isotherm position [22]. Based on the location of markers, a volume fraction of mush  $\phi_{col}$  can be determined in a given finite control volume.

### 2.1.2. Equiaxed nucleation and growth

If non-melting grain refining particles are present within the melt, there is a possibility for nucleation of equiaxed grains within the weld pool away from the columnar solidification front. Nucleants are present because they have been purposely added in the form of grain-refining particles to the weld pool, although in reality they may possibly also result from fragmentation of columnar dendrite arms. Recent work [30] has shown that dendrites bend / bow in the presence of fluid flow. Whether this leads to fragmentation has not been experimentally confirmed and therefore our model takes into account added particles only.

For the modeling of the nucleation and growth of equiaxed grains, we follow a volume averaging approach proposed by Mirihanage and Browne [31]. The minimum diameter of particles that can act as nucleation sites for a given undercooling  $\Delta T_c$  is given by

$$d_{min} = \frac{4\gamma_{sl}}{\Delta S_v \Delta T_c} \quad (5)$$

where  $\gamma_{sl}$  and  $\Delta S_v$  are the solid-liquid interfacial tension and the fusion entropy, respectively.

If the grain refiner particles were equiaxed, we could assume instantaneous nucleation once the necessary undercooling given by equation 5 is reached. More realistically, however, we assume a log-normal distribution of grain refiner particle sizes, with a median  $\mu_{1/2}$  and a unitless standard deviation  $\sigma_d$ . The integral of the probability density function of all particles up to a size  $d_{min}$  gives the cumulative density function

$$F(d_{min}) = \frac{1}{2} \operatorname{erfc}\left(-\frac{\log(d_{min}/\mu_{1/2})}{\sqrt{2}\sigma_d}\right) \quad (6)$$

The number  $N$  of nucleation sites (particles larger than  $d_{min}$ ) in a control volume  $\Delta V$  is then given by

$$N = \rho_{seeds} \Delta V (1 - F(d_{min})) \quad (7)$$

or, in derivative form as

$$\frac{\partial N}{\partial t} = -\rho_{seeds} \Delta V \frac{\partial F(d_{min})}{\partial t} \quad (8)$$

where  $\rho_{seeds}$  is the local number density of grain refiner seeds (seeds per unit volume). The volume of equiaxed grains  $V_{equi}$  within a control volume  $\Delta V$  is given by the number of nucleated grains within  $\Delta V$ , and the volume of each of those grains. The change with time in  $V_{equi}$  can then be written as

$$\frac{\partial V_{equi}}{\partial t} = N \frac{\partial V_{ex}}{\partial t} + \frac{\partial N}{\partial t} V_{nuc}, \quad (9)$$

where  $\partial V_{ex}/\partial t$  is the growth of volume of existing grains and  $V_{nuc}$  is the volume of newly nucleated grains. The growth term can be computed as

$$\frac{\partial V_{ex}}{\partial t} = \frac{4}{3}\pi \frac{d}{dt} R^3 = 4\pi R^2 v \quad (10)$$

The dendrite tip velocity  $v$  is computed using the same analytical growth velocity relationship used in the columnar solidification model (equation 3). The volume averaged dendrite envelope radius  $R$  at a given time can easily be determined as

$$R(t) = \sqrt[3]{\frac{3}{4\pi} \frac{V_{equi}(t)}{N}} \quad (11)$$

From equations (5-11), we may now calculate the temporal evolution of the envelope volume of equiaxed dendrites within the control volume  $\Delta V$  around a location  $(\vec{r}, \Delta V)$ , and from this we may calculate the local equiaxed grain volume fractions as

$$\phi_{equi}^*(\vec{r}) = \frac{V_{equi}(\vec{r}, \Delta V)}{\Delta V(\vec{r})} \quad (12)$$

After some time the equiaxed grains have grown to an extent at which they will start feeling the presence of neighboring grains. To model this so-called grain impingement, we restrict the growth at high volume fractions using an exponential relationship known as the Avrami equation [32]:

$$\phi_{equi} = 1 - \exp(-\phi_{equi}^*) \quad (13)$$

### 2.1.3. Grain transport

Unlike the columnar grains that remain stationary, equiaxed grains are able to move. Since we assume the grains perfectly follow the fluid flow, the grain transport can be computed by the solution of an advection equation for the amount of nucleated grains and the equiaxed volume fraction:

$$\frac{dN}{dt} = \nabla \cdot (\vec{U} N) \quad (14)$$

$$\frac{d\phi_{equi}}{dt} = \nabla \cdot (\vec{U} \phi_{equi}) \quad (15)$$

### 2.1.4. Columnar to equiaxed transition

The columnar front progresses following the growth kinetics given by equation 3 until it meets a coherent equiaxed network. In this case, a columnar to equiaxed transition (CET) may take place, resulting in a different solidification structure. To predict this transition, for every time instance we first compute the growth of equiaxed grains independently of the presence of columnar grains. The volume fraction of the envelope of equiaxed grains is clipped in a way that the sum  $\phi_s = \phi_{equi} + \phi_{col}$  of equiaxed and columnar dendrites does not exceed 1. Now we compute the evolution of the columnar dendrite tips using a mechanical blocking criterion: We assume an equiaxed envelope volume fraction  $\phi_s$  larger than a certain threshold to be coherent in a way that it mechanically blocks further advancement of the columnar dendrite tips. Equiaxed grains that are not bound in a coherent network are integrated into the columnar dendritic network without blocking its progression. There is some variance in the published literature on the choice of the threshold value, ranging from 0.2 [33] to 1 [34]. Since we neglect solutal effects, the mechanical blocking is the only mechanism by which a columnar to equiaxed transition may take place.

### 2.1.5. Latent heat release

The effect of melting and solidification on the heat transfer are taken into account via the source term  $S_{latent}$  in equation 1.

$$S_{latent} = \rho L \frac{dg}{dt} \quad (16)$$

with  $g$  the volume fraction of solid material. While the heat source is active,  $g$  is evaluated as the equilibrium change of volume fraction of solid  $f_s$

$$f_s = \frac{T_l - T}{T_l - T_s}, T_s < T < T_l \quad (17)$$

During the solidification stage, when the heat source is switched off, the solid fraction  $g$  is determined from non-equilibrium solidification kinetics as a combination of the growth of equiaxed and columnar dendrites. The envelope fraction (volume fraction of mush) within a control volume is now given by  $\phi_s = \phi_{col} + \phi_{equi}$ . The solid fraction within

that envelope (the area shaded gray in figure 2) is again denoted by  $f_s$ . Now, the solid fraction  $g$  within a control volume follows from

$$g = \phi_s f_s \quad (18)$$

Equation 17 has been implemented as a linear evolution of the solid fraction between  $T_l$  and  $T_s$ , in order to reduce the computational complexity of the model [26] (avoiding the need for iteration), as in this preliminary model the focus is on successfully coupling both FT and CFD models. A more physically realistic, non-linear relationship, e.g. the Lever Rule or the Scheil equation [35], could be used at the expense of computational efficiency.

### 2.1.6. Coupling of momentum and heat transport

Through the inclusion of the momentum sink term, the momentum equation 2 is valid for the entire domain including both liquid and solid regions. In the (semi-)solid regions, a distinction is made if it is composed of a columnar or equiaxed crystal structure. Columnar dendrites are stationary as they are attached to the unmolten solid, and thus are modeled as a porous medium, introducing a momentum sink following the isotropic Blake-Kozeny model [36]

$$\vec{F}_{damp} = \frac{\mu K}{\rho} \vec{U} \quad (19)$$

$$K = K_0 \frac{g^2}{(1-g)^3 + \epsilon} \quad (20)$$

with  $\mu K_0 = 10^6 \text{ N s}$  and  $\epsilon = 10^{-3}$ .

Equiaxed grains are able to move with the liquid, and with increasing equiaxed volume fraction the liquid metal will turn into a slurry. We model this by increasing the viscosity in the slurry, following a correlation suggested by Thomas [37] for spherical solid particles in a liquid:

$$\mu_{equi} = \mu \left[ 1 + 2.5\phi_{equi}f_s + 10.05(\phi_{equi}f_s)^2 + 0.00273 \exp(16.6\phi_{equi}f_s) \right] \quad (21)$$

This model breaks down when the equiaxed network becomes coherent at high volume fractions. Thus, we switch to the porous medium model for equiaxed regions with a high volume fraction above the coherency threshold.

## 2.2. Boundary conditions

We assume the weld pool to be axisymmetrical and make use of this by only simulating a wedge of the domain. Circumferential gradients and velocities are zero on the wedge faces. The boundary conditions for the other faces are outlined in the following.

### 2.2.1. Heat input

At the top surface, the laser irradiation is modeled by a Gaussian distributed heat flux. At all surfaces, including the top surface, there is an outflux of heat due to natural convection and radiation. This heat outflux is very small compared to the laser irradiation, but once the latter is switched off, it is this heat outflux which together with conduction of excess heat into the unmolten material causes solidification of the weld.

$$\lambda \frac{\partial T}{\partial n} = \dot{q}_{laser} - \dot{q}_{radiation} - \dot{q}_{convection} \quad (22)$$

$$\dot{q}_{radiation} = \sigma_b \epsilon (T^4 - T_\infty^4) \quad (22a)$$

$$\dot{q}_{convection} = h(T - T_\infty) \quad (22b)$$

$$\dot{q}_{laser} = k_q \frac{\eta P}{\pi r_q^2} \exp(-k_q \frac{r^2}{r_q^2}) \quad (22c)$$

The numerical values of the input parameters are given in table 2.

### 2.2.2. Momentum

At the top gas-liquid interface, we introduce a shear stress in the liquid due to surface tension gradients (i.e. Marangoni forces) along the interface:

$$\mu \nabla_n U_t = \frac{d\gamma}{dT} \nabla_t T \quad (23)$$

The variation of surface tension with temperature is computed using the thermochemical model of Sahoo et al. [38].

At all other surfaces, we set the velocity to zero.

## 3. Numerical procedure

Our solver is built on top of the open source finite volume framework OpenFOAM (version 2.1.x) [39]. Postprocessing of the results for publication is done with the open source software matplotlib [40].

The non-linearity associated with the pressure-velocity-coupling is handled by the iterative PISO algorithm [41]. Once a divergence free velocity field has been computed, the temperature equation is solved. If a phase change occurs, the temperature equation will be non-linear and thus solved iteratively. The non-linearity due to latent heat during melting is dealt with using an implicit source term linearization technique [42]. Here, we assume instantaneous progression of the melting front based on local temperature conditions. While this algorithm is appropriate for melting conditions, during solidification it fails to predict undercooling and the metallurgically relevant transition from columnar to equiaxed grain growth. This deficiency is alleviated by using the mesoscale front-tracking

model for solidification predictions by Browne and coworkers [26]. In this case we displace the computational markers forming the solidification front based on the temperature of a previous time step, and then iteratively determine the current temperature and solid fraction within the mushy zone ( $f_s$  in equation 17) with under-relaxation.

Since OpenFOAM can perform 3D simulations only, the solution domain is an axisymmetric wedge of size  $r = 10$  mm and  $z = 5$  mm with an opening angle of  $5^\circ$ . The axisymmetric model presents a marked improvement over previously published 2D planar results e.g. by Duggan et al. [22] or Koseki et al. [24]. For the fluid flow and heat transfer equations, we use a mesh of  $200 \times 100$  uniform cells. For the volume averaged approach to determine equiaxed nucleation and growth we use a mesh that is coarse enough to ensure a reasonable amount of grain refining particles per control volume. Here, we use a uniform mesh of  $160 \times 80$  cells, corresponding to an average of four grain refining particles per grid cell at  $\rho_{seeds} = 1000^{3/2} \text{mm}^{-3}$ . The code is arranged in such a way that the mesh for the fluid flow and heat transfer calculations can be chosen independently from the mesh used for the nucleation and growth calculations. The computations on the two meshes are fully coupled, meaning that data (temperature from macro- to meso-, and solid fraction from meso- to macroscale) is exchanged in both directions at every time step via a linear interpolation framework [2]. This allows for an independent adaptation of the fluid flow and heat transfer mesh to the mesh requirements imposed by the macroscopic length scales.

The time step is fixed at  $25 \mu\text{s}$ . We use a 2nd order backward differencing time marching scheme, and a 2nd order TVD scheme (limitedLinear) for the divergence terms.

## 4. Results and discussion

Following the previous studies by Villafuerte et al. [5, 7], Park [9], Duggan et al. [22] and Koseki et al. [24, 43], we investigate a laser spot weld on an Fe-15.9wt%-Cr-14.1wt%-Ni steel alloy. To determine the growth kinetics coefficient  $C$ , this ternary alloy is treated as a pseudo-binary alloy, as the chromium segregates preferentially to the liquid and the partition coefficient of the nickel is close to 1.0, and thus the chromium is assumed to be the dominant solute [44].

In contrast to previously published computational results, we include fluid flow in our analysis, as it is known to have a strong effect on the heat transfer and shape evolution in a weld pool, both during the melting stage and the solidification stage. The influence of fluid flow on the mesoscale grain structure formation during solidification in welding has not been reported in the literature to date.

### 4.1. Weld evolution during the melting stage

The fluid flow in the pool is driven by surface tension gradients due to temperature gradients. The surface tension dependency on temperature is tightly coupled to the

concentration of surface active agents (surfactants) present in any weld pool, such as sulfur and oxygen. In the following we neglect the presence of oxygen and assume sulfur is the only surfactant (homogeneously) present in the system.

A sketch of the problem investigated is shown in figure 1. The relevant material properties together with their respective literature sources are listed in table 1. The properties related to heat inputs and losses are listed in table 2. For simulations with grain refining particles present, unless otherwise specified we use a TiN particle density of  $(1000/\text{mm}^2)^{3/2}$ , which is the 3D equivalent of a 2D density of  $1000/\text{mm}^2$  as used by Koseki et al. [24]. In their simulations, Koseki et al. assign a homogeneous fixed size of grain refining particles based on a measured required undercooling of  $\Delta T_c = 1.8\text{ K}$  by Bramfitt [8] to achieve nucleation of equiaxed grains on TiN particles. Here, we assume a log-normal distribution of particle sizes (equation 6) as measured by Park [9] with parameters  $\mu_{1/2} = 0.636 \times 10^{-6}\text{ m}$  and  $\sigma_d = 0.1$ , such that the peak of the distribution is close to the value determined by Bramfitt, while the spread of the distribution lies in-between the fixed size assumed by Koseki et al. and the wider log-normal distribution measured by Park.

The high power laser irradiation will lead to melting of the base metal in fractions of a second and thus the formation of a weld pool. For an alloy with a sulfur concentration of 200 ppm the surface tension gradient  $\partial\gamma/\partial T$  is positive for temperatures up to nearly 2100 K (figure 3). Since fluids flow towards regions of higher surface tension, the fluid flow will dominantly be directed towards the center of the pool, where the highest temperatures lead to the highest surface tension. Such a flow pattern leads to a weld pool with a width over depth ratio smaller than 1, characteristic for conduction mode welds (a weld with negligible vaporization of the melt [46]) with a high content of surface active species (figure 4, left column). At lower sulfur concentrations, the sign change of  $\partial\gamma/\partial T$  is shifted towards lower temperatures (figure 3). For a concentration of 80 ppm,  $\partial\gamma/\partial T$  will not remain positive over the entire weld pool surface, and thus the maximum surface tension will not be located at the center of the weld pool but shifted radially outwards, close to the critical 1900 K isotherm. The liquid metal in the weld pool will flow towards this point, leading to two recirculation zones in the weld pool, resulting in decreased penetration with a characteristic bulge of the pool boundary under the stagnation point and a width to depth ratio larger than 1 (figure 4, middle column). The computed maximum velocities in the weld pool are in the order of  $0.3\text{--}0.4\text{ m s}^{-1}$ , which is in good agreement with a maximum velocity of  $[(\partial\gamma/\partial T)q/(\mu c_p)]^{0.5} = 0.3\text{ m s}^{-1}$  obtained by a scaling analysis [47], and simulation results of  $0.4\text{ m s}^{-1}$  for comparable conduction mode laser welds [4].

Here it is illustrative to stress that neglecting fluid flow entirely, as has been done in previous studies [5, 22, 23, 24, 25], leads to a very different, hemispherical weld pool

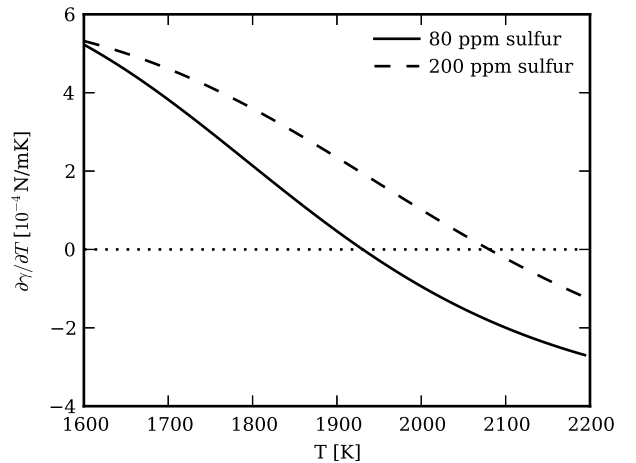


Figure 3: Change of surface tension temperature coefficient with temperature and impurity concentration

shape, irrespective of the sulfur concentration (figure 4, right column). This highlights the need of a proper weld pool flow model to obtain an accurate initial condition for the solidification computations.

#### 4.2. Weld evolution during the solidification stage

Whereas the final shape of the weld is mostly (but not entirely) determined during the heating phase, its grain morphology is fully determined during the cooling phase. Here we study the influence of accounting for solidification kinetics using our front tracking model versus the use of an equilibrium enthalpy method, and the influence of accounting for fluid flow, on the shape and morphology evolution during the cooling stage.

For a 200 ppm sulfur weld, the evolution of the melt pool and temperatures therein, at two time instances after deactivation of the heat source, is shown in figure 5, computed both with the commonly used enthalpy method which does not take into account growth kinetics, and with our combined front-tracking equiaxed growth model. With the latter the temperatures within the weld pool show some difference when compared to the computed temperatures using an enthalpy method. Shown are the  $T_s = 1679\text{ K}$  solidus temperature isotherm and the  $T_l = 1710\text{ K}$  liquidus isotherm. Notable differences are found in the location of the liquidus isotherm and these differences increase during further solidification. In the enthalpy method the solidification front is coincident with the liquidus isotherm, whereas in the front-tracking method the solidification front progression is significantly delayed resulting in a large undercooled region and a much thinner mushy zone. The same conclusion can be drawn for the completely differently shaped weld in a low (80 ppm) sulfur alloy (see figure 6). The transient position of the solidus isotherm with the two models, on the other hand, is virtually the same for both the high and low sulfur case.

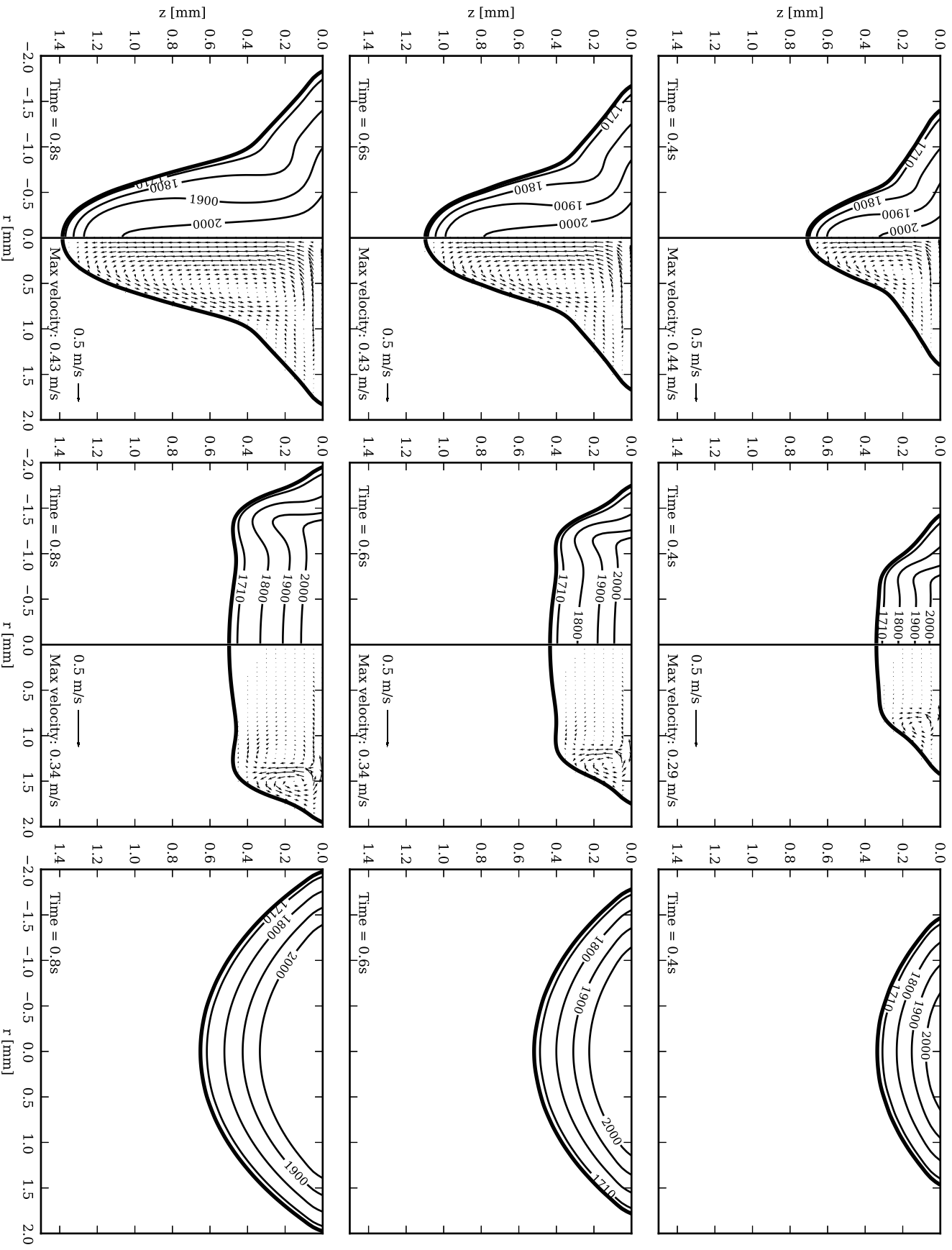


Figure 4: Development of the weld pool with isotherms in Kelvin and flow velocity vectors during the heating stage at three time instances with 200 ppm sulfur (left column), 80 ppm sulfur (middle column) and pure diffusion. The final image shows the state at  $t=0.8s$  when the laser is shut off and solidification begins.

Table 1: Material properties of the Fe-Cr-Ni alloy

Property	Value	Unit	Ref.
Eutectic temperature $T_s$	1679	K	[22]
Liquidus temperature $T_l$	1710	K	[22]
Specific heat capacity $c_p$	780	$\text{J kg}^{-1} \text{K}^{-1}$	[22]
Density $\rho$	7250	$\text{kg m}^{-3}$	[22]
Thermal conductivity $\lambda$	35	$\text{W m}^{-1} \text{K}^{-1}$	[22]
Latent heat of fusion $L$	$1.854 \cdot 10^5$	$\text{J kg}^{-1}$	[22]
Dynamic viscosity $\mu$	$6.1625 \cdot 10^{-3}$	Pa s	[45]
Surface tension temperature coefficient $\partial\gamma/\partial T$	$-4.3 \cdot 10^{-4}$	$\text{N m}^{-1} \text{K}^{-1}$	[38]
Entropy factor	$3.18 \cdot 10^{-3}$	-	[38]
Entropy of segregation	$-1.66 \cdot 10^8$	$\text{J kg}^{-1}$	[38]
Surface excess at saturation	$1.3 \cdot 10^{-8}$	$\text{kmol m}^{-2}$	[38]
Burden and Hunt growth kinetics coefficient $C$	$8.995 \cdot 10^{-5}$	$\text{m s}^{-1} \text{K}^{-2}$	[35]
Diffusivity of Cr in the liquid $D_l$	$1.8 \cdot 10^{-9}$	$\text{m}^2 \text{s}^{-1}$	[35]
Gibbs-Thomson coefficient $\Gamma$	$3.88 \cdot 10^{-7}$	m K	[35]
Liquidus slope $m$	-2.9	K/wt%	[35]
Partition coefficient $\alpha$	0.86	-	[35]
Solid-liquid interfacial tension $\gamma_{sl}$	0.299	$\text{J m}^{-2}$	[22]
Fusion entropy $\Delta S_v$	$7.71 \cdot 10^5$	$\text{J kg}^{-1} \text{K}^{-1}$	[22]

Table 2: Properties related to the laser and heat losses

Property	Value	Unit
Laser power $P$	1000	W
Distribution coefficient $k_q$	2	[-]
Beam radius $r_q$	$2.5 \cdot 10^{-3}$	m
Incidence time	0.8	s
Absorptivity $\eta$	1	[-]
Emissivity $\epsilon$	0.5	[-]
Convective heat transfer coefficient $h$	8	$\text{W m}^{-2} \text{K}^{-1}$
Ambient temperature $T_\infty$	300	K

Thus, simulations aimed solely at predicting the weld pool shape can be carried out with a basic enthalpy method without the need for a sophisticated solidification model. If the post-solidification grain structure is of interest however, a sophisticated solidification model, such as the one presented here, is necessary to compute accurate thermal gradients and solidification front progression, as enthalpy methods have no microstructure information.

The question of the significance of fluid flow during the cooling phase on the evolution of the solidification process is addressed in figures 7 and 8, for high and low sulfur concentrations respectively. For both cases, starting from the same initial condition at the end of the melting phase, the solidification phase is subsequently computed with and without fluid flow. The inclusion of fluid flow in the solidification phase leads to better mixing and heat transfer, and thus lower and more uniform temperatures in the core of the weld pool. This leads to significant differences in the weld pool shape [19, 20], and more importantly in the

post-solidification grain morphology, as will be shown in the next section.

For the high sulfur case, the inclusion of fluid flow, which in this case is directed inward along the weld top surface and downward along the weld axis, leads to continued heat transport to the bottom of the weld after the heat source has been switched off, and thus to continued local melting. This causes a deeper and less wide weld as compared to the situation in which fluid flow is ignored.

For the low sulfur case, the downward fluid flow and convective heat transport is weaker and further away from the axis. Yet, the inclusion of fluid flow leads to continued heat transport to the bottom of the weld after the heat source has been switched off, and a deeper weld as compared to the situation in which fluid flow is ignored.

#### 4.3. Influence of grain refining particles on grain morphology evolution during solidification

Up to this point, we have investigated solidification within the weld pool in the absence of grain refining particles, leading to columnar dendritic growth only. When taking into account the promotion of equiaxed nucleation using grain refiners, at some point the columnar front progression is blocked and the solidification structure transitions into equiaxed grains. This is addressed in the current subsection.

##### 4.3.1. Sensitivity to numerical and model parameters

First, we assess the sensitivity of the main simulation outcome of interest, *viz.* the location of the columnar-equiaxed transition line, as represented by the total volume of equiaxed solid in the weld, on (i) time step and mesh size and (ii) the precise value of the threshold for coherence of equiaxed grains.

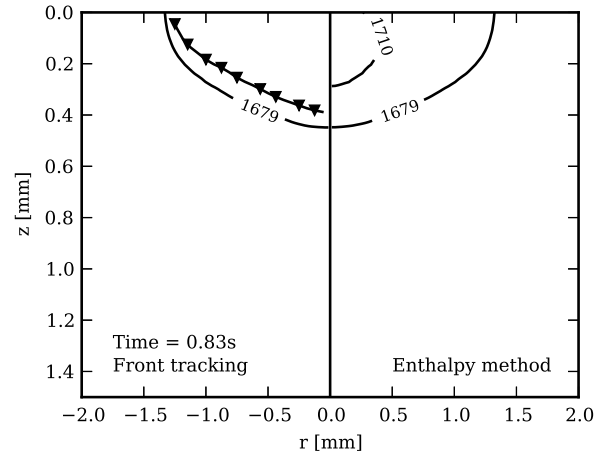
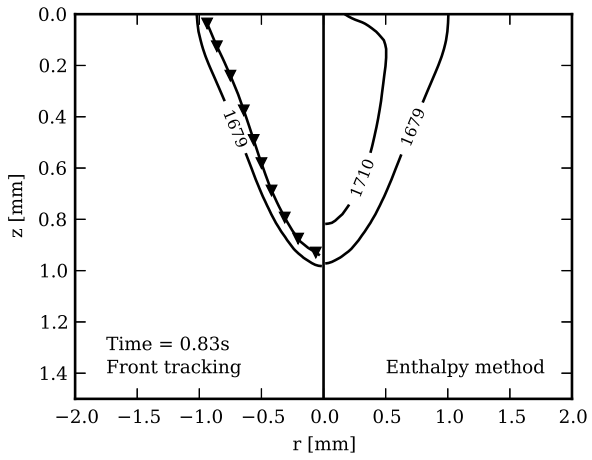
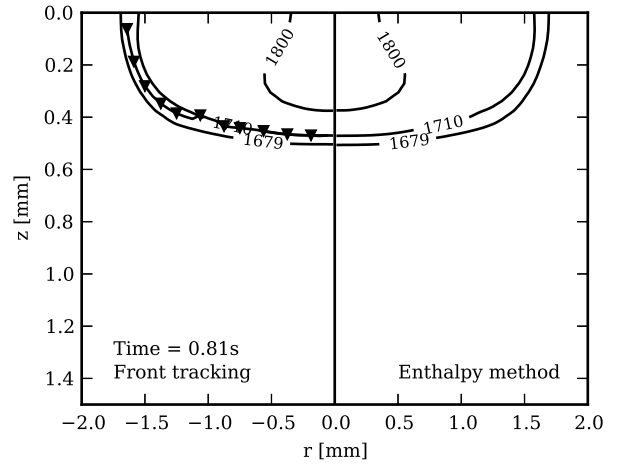
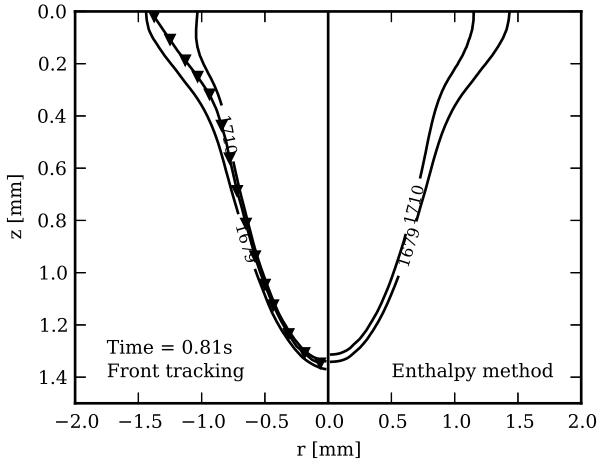


Figure 5: Temperature evolution at two time instances after the heat source has been switched off at  $t=0.80s$ , for 200 ppm sulfur concentration. The location of the columnar dendritic solidification front is depicted by a line with triangle symbols.

Figure 6: Temperature evolution at two time instances after the heat source has been switched off, 80 ppm sulfur

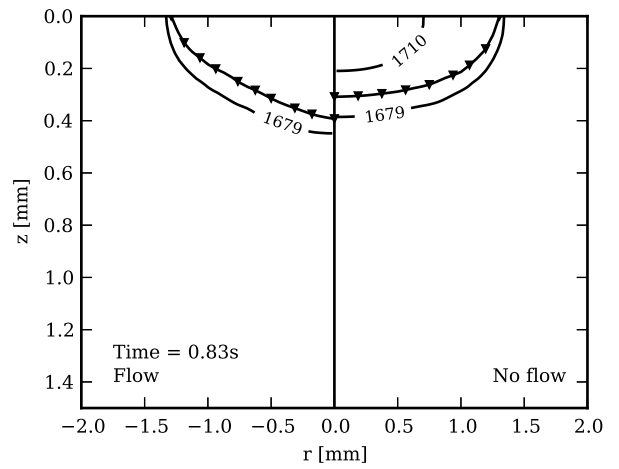
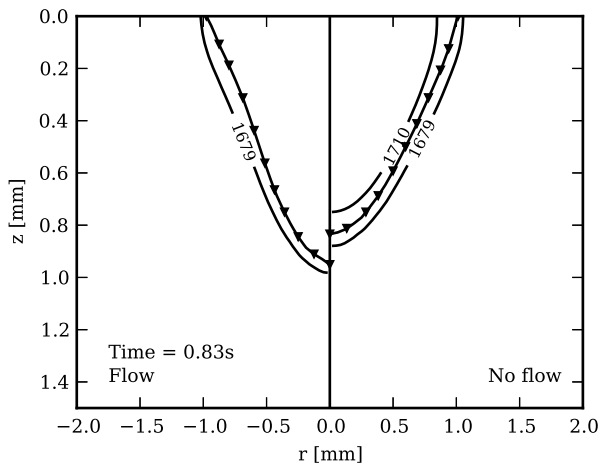
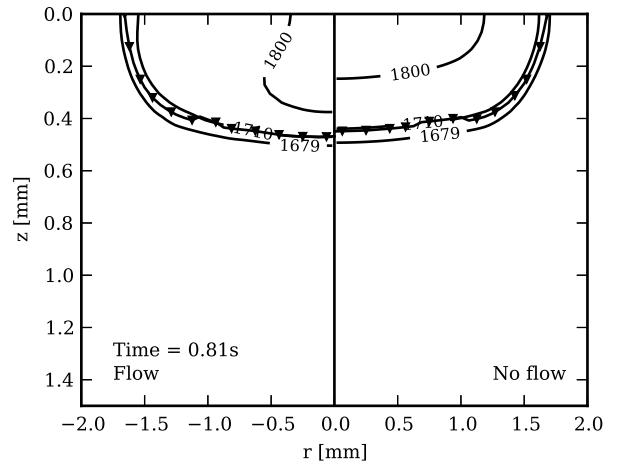
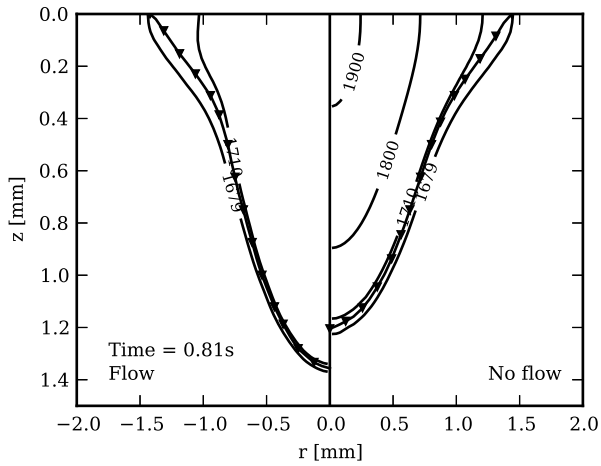


Figure 7: Temperature evolution at two time instances during solidification with and without the consideration of fluid flow, 200 ppm sulfur. The line with triangle symbols depicts the location of the columnar dendritic solidification front.

Figure 8: Temperature evolution at two time instances during solidification with and without the consideration of fluid flow, 80 ppm sulfur. The line with triangle symbols depicts the location of the columnar dendritic solidification front.

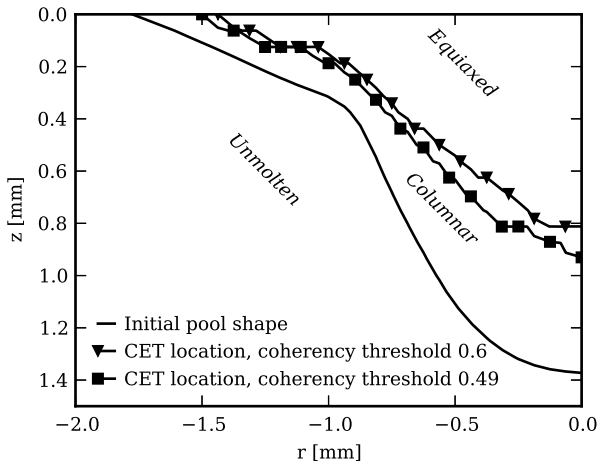


Figure 9: Sensitivity on the coherency threshold of the computed transition from columnar to equiaxed solidification structure in a weld pool, 200 ppm sulfur

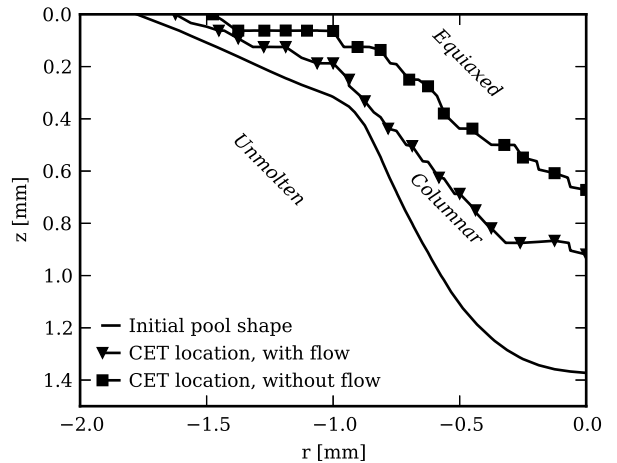


Figure 10: Equiaxed transition in a weld pool with and without fluid flow, 200 ppm sulfur

Ad (i): A simulation with a doubled fixed time step of  $50 \mu\text{s}$  resulted in a slight increase of 4.6% of the volume of equiaxed solid (and a corresponding decrease in the volume of columnar dendritic solid). The total volumes of equiaxed solid in the weld, as computed with a fixed time step of  $25 \mu\text{s}$  on three different meshes, *viz.* the standard mesh, and two meshes that are coarsened and refined by a linear factor 1.25 compared to the standard mesh (see Roache [48] for a justification of the refinement ratio), show a monotonic convergence, allowing for the computation of an asymptotic value by Richardson extrapolation. Compared to the asymptotic value, the coarse mesh result is 6.1% smaller, the base mesh result 2.0% smaller and the fine mesh result 0.48% smaller.

Ad (ii): In a previous section, we mentioned that the precise value of the threshold for coherence of the equiaxed grains is not agreed upon in the literature (ranging from 0.2 [33] to 1 [34]). To study the sensitivity of our results to this threshold value, we simulated solidification of a weld pool using a coherency threshold of 0.49 and 0.6, leading to a 15% difference in the volume of equiaxed structure in the weld (figure 9). The same conclusion has been drawn by Mirihanage and Browne [31], who found the occurrence of the columnar-to-equiaxed transition (CET) in a casting to be rather insensitive to the exact value of the coherency threshold. All further simulations in the current study were performed with the most commonly used blocking threshold of 0.49 as proposed by Hunt [49].

#### 4.3.2. Influence of grain transport

The presence of fluid flow in the weld pool during solidification leads to a significantly earlier transition to equiaxed growth, as can be seen in figures 10 and 11 for high and low sulfur cases respectively. Conversely, the location of the columnar-to-equiaxed transition was found to be rather insensitive to the inclusion or neglect of the

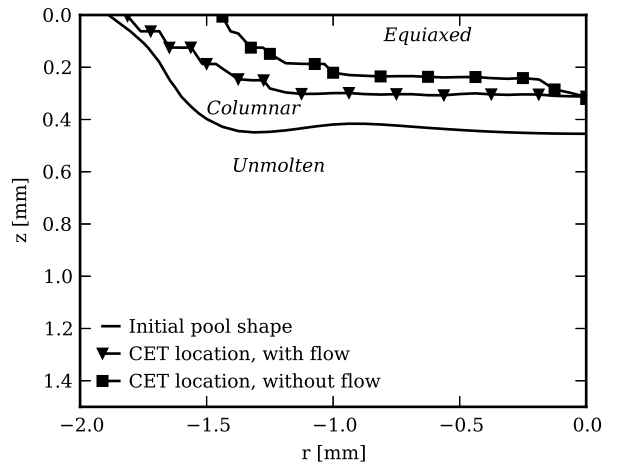


Figure 11: Equiaxed transition in a weld pool with and without fluid flow, 80 ppm sulfur

transport of equiaxed grains with the flow, as described by equations 14 and 15.

Hence, the earlier transition to equiaxed growth when including fluid flow is mainly due to the lower thermal gradients and lower temperatures in the melt (see figure 7), which result in a larger liquid region with sufficient undercooling for the equiaxed nucleation and growth to take place. This conclusion agrees with Hunt's criterion [49], stating that the fraction of equiaxed grains is inversely proportional to the magnitude of the thermal gradients cubed in the melt.

#### 4.3.3. Influence of grain refining particle number density

The influence of the number density of grain refining particles on the transition from columnar to equiaxed solidification is illustrated in figures 12 and 13, which show that the transition to equiaxed solidification can be triggered with a grain refiner density of  $500^{3/2}$  particles per

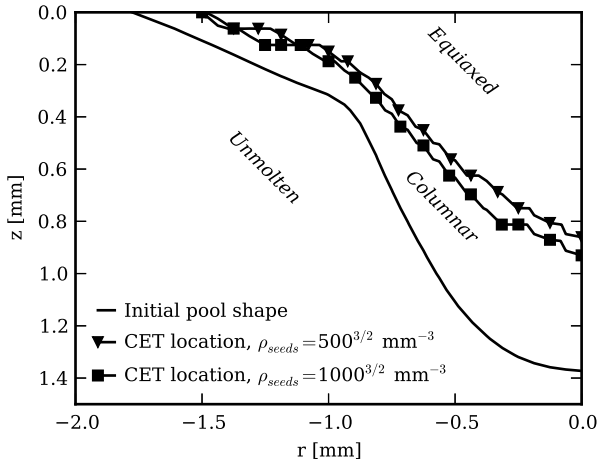


Figure 12: Equiaxed transition in a weld pool with two different densities of grain refining particles, 200 ppm sulfur

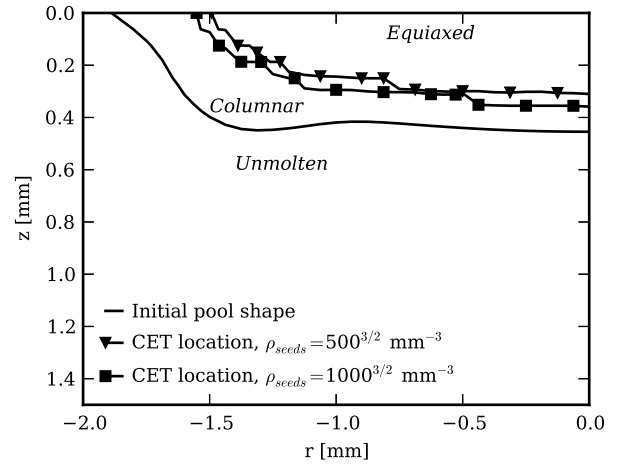


Figure 13: Equiaxed transition in a weld pool with two different densities of grain refining particles, 80 ppm sulfur

$\text{mm}^3$ , and that the position of the transition is only slightly affected by an increase of the grain refiner number density to  $1000^{3/2}$  particles per  $\text{mm}^3$ . This observation matches the findings by Koseki et al. [24] that grain refiner density mainly influences the size of the resulting equiaxed grains, and not the point at which they reach coherency. Simulating the effect of a grain refiner density lower than  $500^{3/2}$  particles per  $\text{mm}^3$  is not feasible using our current volume averaged approach, as this would require very large computational cells in relation to the weld pool area to allow for a sufficient number of grain refiner particles per computational cell. In figures 14 and 15, we show the thermal gradient and equiaxed envelope volume along a diagonal line  $r_{\perp} = \sqrt{r^2 + z^2}$ ,  $z = r$  at a time instance where the equiaxed grains reach coherency. We can identify a low, fairly uniform temperature gradient within the weld pool which rises sharply around the liquid-solid interface and is insensitive to the number of grain refining particles present. As a result, favorable conditions for the growth of equiaxed grains are met at the same location for both particle densities, though coherency is achieved slightly later in time for the lower number density.

## 5. Conclusion

In addition to the macroscopic shape of a weld, the mesoscopic grain morphology is crucial in determining the resultant properties. These two are determined by the interaction between macroscale fluid flow and heat transfer, and mesoscale grain solidification kinetics, during the heating and cooling phase of a welding process. Whereas both macroscale and mesoscale phenomena have previously been studied separately through computational models, an integrated model for both scales is needed to predict weld properties on both relevant scales.

Such an integrated model has been presented in the current work. The model is conceptually simple and com-

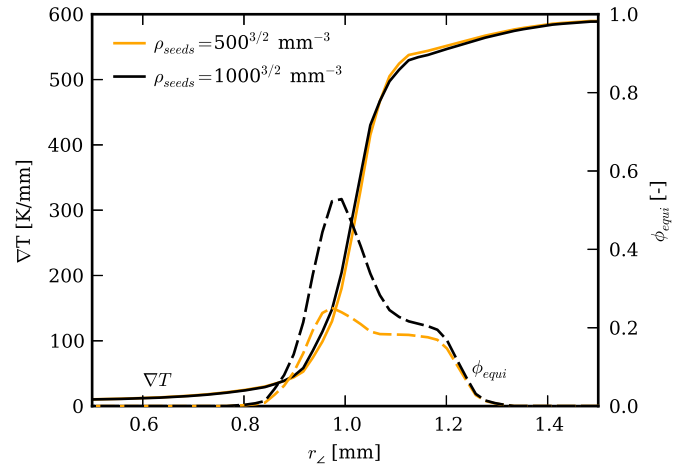


Figure 14: Thermal gradient and equiaxed envelope volume fraction along a diagonal line  $z = r$  away from the weld pool center, 200 ppm

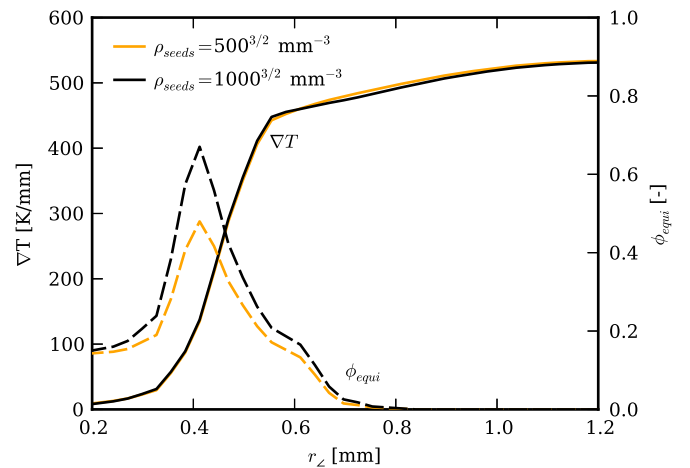


Figure 15: Thermal gradient and equiaxed envelope volume fraction along a diagonal line  $z = r$  away from the weld pool center, 80 ppm

putationally inexpensive, while granting insight into the post-solidification shape and grain morphology of a weld.

The model has been applied to study the melting and solidification of a laser spot weld on two Fe-Cr-Ni steel alloys, *viz.* with a low and high sulfur content. Due to their very different dependency of surface tension on temperature, the weld pools of these two alloys represent the two extremes in surface tension driven flow commonly observed during welding. Although demonstrated here for laser spot welding, the presented results are relevant for arc welding as well, as both types of welding are equivalent once the heat source is turned off.

The predicted solidification evolution has been compared to that obtained with the commonly used equilibrium enthalpy method, in which solidification takes place quasi-statically and its kinetics is ignored. Apart from the obvious fact that an equilibrium method cannot predict the important transitions in grain morphology, a marked difference between the two methods was observed in the thermal gradients within the weld pool during solidification. This in turn has a strong impact on the developing grain structure. However, if only the weld pool shape, and not its grain morphology, is of interest, the equilibrium enthalpy method is found to be sufficient to obtain accurate results for the partial penetration cases examined here.

Neglecting fluid flow during the cooling phase, as done in previously reported studies, was found to have a significant influence on the predicted weld pool shape and grain morphology. Thus any accurate simulation of weld pools should include fluid flow.

The use of grain refining particles was found to be an effective means to favorably alter the grain morphology by initiating a transition from columnar to equiaxed growth. This transition was found to be not very sensitive to the most uncertain parameter in the model, *viz.* the coherency threshold value, nor to the density of grain refining particles above a certain critical value.

## Acknowledgments

We would like to thank the European Commission for funding the MINTWELD project (reference 229108) via the FP7-NMP program.

## References

### References

### References

- [1] W. Moos, R. Janßen-Timmen, J. Klöpper, N. Leonenko, Gesamtwirtschaftliche und sektorale Wertschöpfung aus der Produktion und Anwendung von Füge-technik in Deutschland und Europa, *Schweißen&Schneiden* 65 (9) (2013) 572–584.
- [2] M. Tong, G. Duggan, J. Liu, Y. Xie, M. Dodge, L. Aucott, H. Dong, R. L. Davidchack, J. Dantzig, O. Barrera, A. C. F. Cocks, H. Kitaguchi, S. Lozano-Perez, C. Zhao, I. M. Richardson, A. Kidess, C. R. Kleijn, S. Wen, R. Barnett, D. J. Browne, Multiscale, Multiphysics Numerical Modeling of Fusion Welding with Experimental Characterization and Validation, *JOM* 65 (1) (2013) 99–106, ISSN 1047-4838, doi:10.1007/s11837-012-0499-6.
- [3] C. R. Heiple, J. R. Roper, Mechanism for minor element effect on GTA fusion zone geometry, *Welding Journal* 61 (4) (1982) 97–s–102–s.
- [4] W. Pitscheneder, T. DebRoy, K. Mundra, R. Ebner, Role of sulfur and processing variables on the temporal evolution of weld pool geometry during multikilowatt laser beam welding of steels, *Welding Journal* 75 (3) (1996) 71–s–80–s.
- [5] J. C. Villafuerte, E. Pardo, H. W. Kerr, The effect of alloy composition and welding conditions on columnar-equiaxed transitions in ferritic stainless steel gas-tungsten arc welds, *Metallurgical Transactions A* 21 (7) (1990) 2009–2019, doi:10.1007/bf02647249.
- [6] G. J. Davies, J. G. Garland, Solidification Structures and Properties of Fusion Welds, *International Materials Reviews* 20 (1) (1975) 83–108, ISSN 0950-6608, doi:10.1179/imr.1975.20.1.83.
- [7] J. C. Villafuerte, H. W. Kerr, S. A. David, Mechanisms of equiaxed grain formation in ferritic stainless steel gas tungsten arc welds, *Materials Science and Engineering: A* 194 (2) (1995) 187–191, ISSN 09215093, doi:10.1016/0921-5093(94)09656-2.
- [8] B. L. Bramfitt, The effect of carbide and nitride additions on the heterogeneous nucleation behavior of liquid iron, *Metallurgical Transactions* 1 (7) (1970) 1987–1995, doi:10.1007/bf02642799.
- [9] J. H. Park, Effect of inclusions on the solidification structures of ferritic stainless steel: Computational and experimental study of inclusion evolution, *Calphad* 35 (4) (2011) 455–462, ISSN 03645916, doi:10.1016/j.calphad.2011.08.004.
- [10] M. Gäumann, W. Kurz, Why is it so difficult to produce an equiaxed microstructure during welding?, in: H. Cerjak, H. K. D. H. Bhadeshia (Eds.), *Mathematical Modelling of Weld Phenomena 4*, Materials Modelling Series, The Institute of Materials, IOM Communications, London, ISBN 1-86125-060-6, 125–136, 1997.
- [11] F. C. Campbell, Defects leading to failure, chap. A.8.6.1, *ASM International*, Materials Park, Ohio, ISBN 978-1-62198-373-6, 619+, 2012.
- [12] S. A. David, J. M. Vitek, Correlation between solidification parameters and weld microstructures, *International Materials Reviews* 34 (1) (1989) 213–245, ISSN 0950-6608, doi:10.1179/imr.1989.34.1.213.
- [13] J. A. Spittle, Columnar to equiaxed grain transition in as solidified alloys, *International Materials Reviews* 51 (4) (2006) 247–269, ISSN 0950-6608, doi:10.1179/174328006x102493.
- [14] W. U. Mirihanage, H. Dai, H. Dong, D. J. Browne, Computational Modeling of Columnar to Equiaxed Transition in Alloy Solidification, *Adv. Eng. Mater.* 15 (4) (2013) 216–229, doi:10.1002/adem.201200220.
- [15] E.-J. Ha, W.-S. Kim, A study of low-power density laser welding process with evolution of free surface, *International Journal of Heat and Fluid Flow* 26 (4) (2005) 613–621, ISSN 0142727X, doi:10.1016/j.ijheatfluidflow.2005.03.009.
- [16] M. Kanouff, R. Greif, The unsteady development of a GTA weld pool, *International Journal of Heat and Mass Transfer* 35 (4) (1992) 967–979, ISSN 00179310, doi:10.1016/0017-9310(92)90261-p.
- [17] Y. P. Lei, H. Murakawa, Y. W. Shi, X. Y. Li, Numerical analysis of the competitive influence of Marangoni flow and evaporation on heat surface temperature and molten pool shape in laser surface remelting, *Computational Materials Science* 21 (3) (2001) 276–290, ISSN 09270256, doi:10.1016/s0927-0256(01)00143-4.
- [18] W. Zhang, G. G. Roy, J. W. Elmer, T. DebRoy, Modeling of heat transfer and fluid flow during gas tungsten arc spot welding of low carbon steel, *Journal of Applied Physics* 93 (5) (2003) 3022–3033, doi:10.1063/1.1540744.
- [19] G. Ehlen, A. Ludwig, P. R. Sahn, Simulation of time-dependent pool shape during laser spot welding: Transient effects, *Metallurgical and Materials Transactions A* 34 (12) (2003) 2947–2961, ISSN 1073-5623, doi:10.1007/s11661-003-0194-x.
- [20] Z. S. Saldi, A. Kidess, S. Kenjereš, C. Zhao, I. M. Richardson, C. R. Kleijn, Effect of enhanced heat and mass trans-

- port and flow reversal during cool down on weld pool shapes in laser spot welding of steel, *International Journal of Heat and Mass Transfer* 66 (2013) 879–888, ISSN 00179310, doi:10.1016/j.ijheatmasstransfer.2013.07.085.
- [21] S. Chen, G. Guillemot, C.-A. Gandin, 3D Coupled Cellular Automaton (CA)-Finite Element (FE) Modeling for Solidification Grain Structures in Gas Tungsten Arc Welding (GTAW), *ISIJ International* 54 (2) (2014) 401–407, ISSN 0915-1559, doi:10.2355/isijinternational.54.401.
- [22] G. Duggan, W. U. Mirihanage, M. Tong, D. J. Browne, A combined enthalpy / front tracking method for modelling melting and solidification in laser welding, *IOP Conference Series: Materials Science and Engineering* 33 (1) (2012) 012026+, ISSN 1757-899X, doi:10.1088/1757-899x/33/1/012026.
- [23] G. Duggan, M. Tong, D. J. Browne, An integrated meso-scale numerical model of melting and solidification in laser welding, *IOP Conference Series: Materials Science and Engineering* 27 (1) (2012) 012077+, ISSN 1757-899X, doi:10.1088/1757-899x/27/1/012077.
- [24] T. Koseki, H. Inoue, Y. Fukuda, A. Nogami, Numerical simulation of equiaxed grain formation in weld solidification, *Science and Technology of Advanced Materials* 4 (2) (2003) 183–195, ISSN 1468-6996, doi:10.1016/s1468-6996(03)00026-3.
- [25] X. H. Zhan, Z. B. Dong, Y. H. Wei, Y. L. Xu, Dendritic grain growth simulation in weld molten pool based on CA-FD model, *Cryst. Res. Technol.* 43 (3) (2008) 253–259, doi:10.1002/crat.200710966.
- [26] D. J. Browne, J. D. Hunt, A fixed grid front-tracking model of the growth of a columnar front and an equiaxed grain during solidification of an alloy, *Numerical Heat Transfer, Part B: Fundamentals* 45 (5) (2004) 395–419, doi:10.1080/10407790490430606.
- [27] M. H. Burden, J. D. Hunt, Cellular and dendritic growth. II, *Journal of Crystal Growth* 22 (2) (1974) 109–116, ISSN 00220248, doi:10.1016/0022-0248(74)90127-4.
- [28] W. Kurz, B. Giovanola, R. Trivedi, Theory of microstructural development during rapid solidification, *Acta Metallurgica* 34 (5) (1986) 823–830, ISSN 00016160, doi:10.1016/0001-6160(86)90056-8.
- [29] J. S. Langer, J. Müller-Krumbhaar, Stability effects in dendritic crystal growth, *Journal of Crystal Growth* 42 (1977) 11–14, ISSN 00220248, doi:10.1016/0022-0248(77)90171-3.
- [30] W. U. Mirihanage, K. V. Falch, I. Snigireva, A. Snigirev, Y. J. Li, L. Arnberg, R. H. Mathiesen, Retrieval of three-dimensional spatial information from fast in situ two-dimensional synchrotron radiography of solidification microstructure evolution, *Acta Materialia* 81 (2014) 241–247, ISSN 13596454, doi:10.1016/j.actamat.2014.08.016.
- [31] W. U. Mirihanage, D. J. Browne, Combined analytical/numerical modelling of nucleation and growth during equiaxed solidification under the influence of thermal convection, *Computational Materials Science* 46 (4) (2009) 777–784, ISSN 09270256, doi:10.1016/j.commatsci.2009.04.016.
- [32] J. W. Christian, *The Theory of Transformations in Metals and Alloys (Part I + II): v. 1-2*, Pergamon, 1 edn., 2002.
- [33] V. B. Biscuola, M. A. Martorano, Mechanical Blocking Mechanism for the Columnar to Equiaxed Transition, *Metallurgical and Materials Transactions A* 39 (12) (2008) 2885–2895, doi:10.1007/s11661-008-9643-x.
- [34] W. Mirihanage, S. McFadden, D. J. Browne, Macroscopic Model for Predicting Columnar to Equiaxed Transitions Using Columnar Front Tracking and Average Equiaxed Growth, *Materials Science Forum* 649 (2010) 355–360, ISSN 1662-9752, doi:10.4028/www.scientific.net/msf.649.355.
- [35] G. Duggan, M. Tong, D. J. Browne, Modelling the creation and destruction of columnar and equiaxed zones during solidification and melting in multi-pass welding of steel, *Computational Materials Science* 97 (2015) 285–294, ISSN 09270256, doi:10.1016/j.commatsci.2014.09.022.
- [36] A. Singh, R. Pardeshi, B. Basu, Modelling of convection during solidification of metal and alloys, *Sadhana* 26 (1) (2001) 139–162, ISSN 0256-2499, doi:10.1007/bf02728483.
- [37] D. G. Thomas, Transport characteristics of suspension: VIII. A note on the viscosity of Newtonian suspensions of uniform spherical particles, *Journal of Colloid Science* 20 (3) (1965) 267–277, ISSN 00958522, doi:10.1016/0095-8522(65)90016-4.
- [38] P. Sahoo, T. Debroy, M. McNallan, Surface tension of binary metal - surface active solute systems under conditions relevant to welding metallurgy, *Metallurgical and Materials Transactions B* 19 (3) (1988) 483–491–491, ISSN 0360-2141, doi:10.1007/bf02657748.
- [39] H. G. Weller, G. Tabor, H. Jasak, C. Fureby, A tensorial approach to computational continuum mechanics using object-oriented techniques, *Computers in Physics* 12 (6) (1998) 620–631, doi:10.1063/1.168744.
- [40] J. D. Hunter, Matplotlib: A 2D Graphics Environment, *Computing in Science and Engineering* 9 (3) (2007) 90–95, ISSN 1521-9615, doi:10.1109/mcse.2007.55.
- [41] R. I. Issa, Solution of the implicitly discretised fluid flow equations by operator-splitting, *Journal of Computational Physics* 62 (1) (1986) 40–65, ISSN 00219991, doi:10.1016/0021-9991(86)90099-9.
- [42] V. R. Voller, C. R. Swaminathan, General source-based method for solidification phase change, *Numerical Heat Transfer, Part B: Fundamentals: An International Journal of Computation and Methodology* 19 (2) (1991) 175–189, doi:10.1080/10407799108944962.
- [43] T. Koseki, H. Inoue, A. Nogami, Y. Fukuda, Columnar-To-Equiaxed Transition during Solidification of Steel Welds, in: S. A. David (Ed.), *6th International Trends in Welding Research Conference Proceedings, Trends in Welding Research, ASM International, ASM International, ISBN 9781615032518* 1615032517, 35–40, 2002.
- [44] J. W. Elmer, T. W. Eager, S. M. Allen, Single-phase solidification during rapid resolidification of stainless steel alloys, in: *Proc. of the Materials Weldability Symposium, ASM International, Materials Park, OH, 143, 143–150*, 1990.
- [45] R. F. Brooks, A. T. Dinsdale, P. N. Quedest, The measurement of viscosity of alloys - a review of methods, data and models, *Measurement Science and Technology* 16 (2) (2005) 354+, ISSN 0957-0233, doi:10.1088/0957-0233/16/2/005.
- [46] T. J. Lienert, S. S. Babu, T. A. Siewert, V. L. Acoff, *Laser beam welding, ASM International, ISBN 978-1-61344-660-7, 558+*, 2011.
- [47] S. Chakraborty, S. Sarkar, P. Dutta, Scaling analysis of momentum and heat transport in gas tungsten arc weld pools, *Science and Technology of Welding and Joining* 7 (2) (2002) 88–94, ISSN 13621718, doi:10.1179/136217102225001322.
- [48] P. J. Roache, Perspective: A Method for Uniform Reporting of Grid Refinement Studies, *Journal of Fluids Engineering* 116 (3) (1994) 405–413, doi:10.1115/1.2910291.
- [49] J. D. Hunt, Steady state columnar and equiaxed growth of dendrites and eutectic, *Materials Science and Engineering* 65 (1) (1984) 75–83, ISSN 00255416, doi:10.1016/0025-5416(84)90201-5.